




Transverse optical binding for a dual dipolar dielectric nanoparticle dimerXiao-Yong Duan ^{1,2,*}, Graham D. Bruce ², Kishan Dholakia ^{2,3}, Zhi-Guo Wang,⁴ Feng Li,¹ and Ya-Ping Yang⁵¹*School of Mathematics, Physics and Information Engineering, Jiaxing University, Jiaxing 314001, China*²*SUPA School of Physics and Astronomy, University of St Andrews, St Andrews, KY16 9SS, United Kingdom*³*Department of Physics, College of Science, Yonsei University, Seoul 03722, South Korea*⁴*School of Physics Science and Engineering, Tongji University, Shanghai 200092, China*⁵*School of Design, Jiaxing University, Jiaxing 314001, China*

(Received 23 November 2019; accepted 23 December 2020; published 19 January 2021)

The physical origins of the transverse optical binding force and torque beyond the Rayleigh approximation have not been clearly expressed to date. Here, we present analytical expressions of the force and torque for a dual dipolar dielectric dimer illuminated by a plane wave propagating perpendicularly to the dimer axis. Using this analytical model, we explore the roles of the hybridized electric dipolar, magnetic dipolar, and electric-magnetic dipolar coupling interactions in the total force and torque on the particles. We find significant departures from the predictions of the Rayleigh approximation, particularly for high-refractive-index particles, where the force is governed by the magnetic interaction. This results in an enhancement of the dimer stability by one to four orders of magnitude compared to the predictions of the Rayleigh approximation. For the case of torque, this is dominated by the coupling interaction and increases by an order of magnitude. Our results will help to guide future experimental work in optical binding of high-refractive-index dielectric particles.

DOI: [10.1103/PhysRevA.103.013721](https://doi.org/10.1103/PhysRevA.103.013721)**I. INTRODUCTION**

Optical binding originating from the mutual scattering of electromagnetic (EM) waves among objects enables micro- and nanoparticles to form stable spatial arrangements. Therefore, it has attracted great attention in light-controlled self-assembly of particles [1,2]. For a pair of particles (or dimer), when the incident light wave vector is *perpendicular* to the dimer axis, the resulting force between particles is named the transverse optical binding force (TOBF) [3]. For the case of the light wave propagating *along* the dimer axis, the force is termed the longitudinal optical binding force [4].

TOBF offers a way to assemble dielectric and metallic particles into complex steady structures, such as one-dimensional chains [3] and waveguides [5], two-dimensional optical matter [6,7], clusters [8], arrays [9–11], mirrors [12], and three-dimensional clusters [13]. Furthermore, it can dynamically manipulate particles, e.g., inducing oscillations in particle chains [14], rotation and spinning of particles [15,16], and forming a bound state of two rotating microscopes [17]. Currently, an emerging research field is the dependence of the TOBF on EM hybridization coming from the interaction between electric and/or magnetic multipoles in adjacent particles. In detail, the sign of the TOBF in a silver disk-ring nanostructure reverses multiply due to the hybridized interference between the electric dipole of disk and the electric high-order modes of the ring [18]. Analogous phenomena were found in Au nanorod heterodimers [19]. Further numerical results showed that the TOBF for a silicon dimer changes

from an attractive force to a repulsive one with variation of wavelength [20]. The repulsive force originates from the hybridization between the broad electric dipole and narrow magnetic dipole in the particles. Recent theory indicated that TOBF induced by the interference of surface plasmon polarizations (SPPs) of two metallic particles over a metallic substrate is an order of magnitude larger than the TOBF without SPPs [21].

While the TOBF is well studied for low-refractive-index dielectric (index < 2.5 , e.g., polystyrene and glass) and metallic particles in the Rayleigh approximation [15,22], optical binding for high-refractive-index dielectric particles with $n > 3.5$, such as silicon and germanium, has received little attention because analytical solutions of the TOBF beyond the Rayleigh approximation have remained absent [1,23,24]. Such particles are of interest in the area of dielectric metamaterials, where they can be harnessed for optical devices without the high heating rates associated with plasmonic particles [25], and in optical trapping because their strong oscillatory dynamics can be utilized as a thermal engine [26]. Further, their morphology can be manipulated to customize their form birefringence to provide optical microfluidic actuators [27], and they can be used to create nanoheterostructure semiconductor devices [28]. In this paper, we analytically study the TOBF and torque on two dual dipolar dielectric particles orthogonally illuminated by an arbitrarily polarized plane EM wave, as shown in Fig. 1. We show that the contributions to the force and torque due to electric dipolar, to magnetic dipolar, and to electric-magnetic dipolar coupling interactions are dominant in different regimes of refractive index, and therefore are essential for the full description of the TOBF, going beyond the Rayleigh approximation.

*Corresponding author: xyduan@zjxu.edu.cn

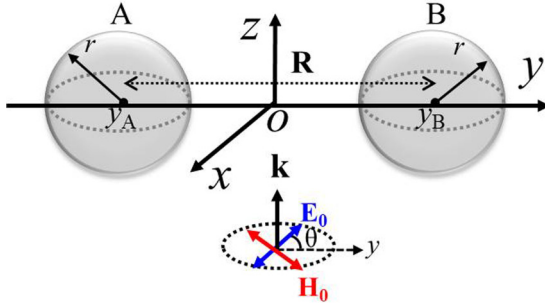


FIG. 1. A pair of dielectric spheres with radius r located symmetrically at positions y_A and y_B along the y axis of a Cartesian system (O - xyz). R represents the distance between the centers of the two particles. A plane EM wave with electric (\mathbf{E}_0) and magnetic (\mathbf{H}_0) field vectors is incident on the dimer along the z axis, as shown by the wave vector \mathbf{k} . θ is the polarization angle of the wave, measured between the \mathbf{E}_0 and y axis.

The paper is organized as follows. In Sec. II, we present the results of our derivation of analytical expressions for the TOBF and optical torque. Meanwhile, the physical meanings of the expressions are discussed. In Sec. III, the contributions of the electric dipolar, magnetic dipolar, and electric-magnetic dipolar coupling interactions to TOBF, torque, and stability of the dimer are numerically investigated in detail. Finally, conclusions are drawn in Sec. IV.

II. THEORETICAL MODEL

Based on the optical force on a single dual dipolar particle [29] and EM mutual scattering between two particles [30] (see details in Appendixes A–F), we derive the TOBF (F) (exerted along the y axis in Fig. 1) on particle B , which is equal but oppositely directed to the force on particle A . F consists of three parts:

$$F_e = \frac{\varepsilon_0 \varepsilon_s}{2} \left\{ \begin{aligned} & \left(\text{Re} \left[\frac{\partial \kappa}{\partial R} \right] |\tilde{\alpha}_{ey}|^2 - \text{Re} \left[\frac{\partial \mu}{\partial R} \right] |\tilde{\alpha}_{em-p,1}|^2 + \text{Re} \left[\frac{\partial \eta}{\partial R} \tilde{\alpha}_{em-p,2} \tilde{\alpha}_{em-p,1}^* \right] \right) |E_{0,y}|^2 \\ & + \left(\text{Re} \left[\frac{\partial \eta}{\partial R} \tilde{\alpha}_{em-s,1} \tilde{\alpha}_{em-s,2}^* \right] + \text{Re} \left[\frac{\partial \mu}{\partial R} \right] |\tilde{\alpha}_{em-s,2}|^2 \right) |E_{0,x}|^2 \end{aligned} \right\}, \quad (1)$$

$$F_m = \frac{\varepsilon_0 \varepsilon_s}{2} \left\{ \begin{aligned} & \left(\text{Re} \left[\frac{\partial \mu}{\partial R} \right] |\tilde{\alpha}_{em-p,2}|^2 + \text{Re} \left[\frac{\partial \eta}{\partial R} \tilde{\alpha}_{em-p,1} \tilde{\alpha}_{em-p,2}^* \right] \right) |E_{0,y}|^2 \\ & + \left(\text{Re} \left[\frac{\partial \kappa}{\partial R} \right] |\tilde{\alpha}_{my}|^2 - \text{Re} \left[\frac{\partial \mu}{\partial R} \right] |\tilde{\alpha}_{em-s,1}|^2 + \text{Re} \left[\frac{\partial \eta}{\partial R} \tilde{\alpha}_{em-s,2} \tilde{\alpha}_{em-s,1}^* \right] \right) |E_{0,x}|^2 \end{aligned} \right\}, \quad (2)$$

$$F_{em} = \frac{\varepsilon_0 \varepsilon_s}{12\pi} k^4 \text{Im} \left[\tilde{\alpha}_{em-p,1} \tilde{\alpha}_{em-p,2}^* |E_{0,y}|^2 - \tilde{\alpha}_{em-s,1}^* \tilde{\alpha}_{em-s,2} |E_{0,x}|^2 \right], \quad (3)$$

where Re and Im represent the real and imaginary parts of a complex number, $*$ denotes complex conjugation, ε_0 and ε_s are respectively the permittivity of vacuum and relative permittivity of the medium, $E_{0,x}$ and $E_{0,y}$ are x and y components of the incident electric field, R is the distance between the centers of the two particles, $\partial/\partial R$ denotes the partial derivative with respect to the distance, $k = 2\pi/\lambda_s$ is the wave number in the medium, and the dressed polarizabilities $\tilde{\alpha}_{ey}$, $\tilde{\alpha}_{my}$, $\tilde{\alpha}_{em-p,1}$, $\tilde{\alpha}_{em-p,2}$, $\tilde{\alpha}_{em-s,1}$, and $\tilde{\alpha}_{em-s,2}$ represent the polarization of the particle induced by the incident light and hybridization while μ , κ , and η are eigenvalues of electric and magnetic dyadic Green's functions of a point dipole (see details in Appendixes A and B).

F_e is the electric component of F . The first term denotes the interaction between the y components of the electric dipole moments (p_y) of the two particles, while the second term is the interaction between the z components of the electric dipole moments (p_z). The third term is the force on the z component of the electric dipole moment in particle B (p_z^B) acted on by the x component of the magnetic dipole moment in particle A (m_x^A). The combination of these first three terms (in the first parentheses) represents F_e in the case of illumination by p polarization (i.e., along the dimer axis). The fourth term is the interaction between the two p_x while the last one denotes the force exerted on p_x^B by m_z^A . These last two terms (in the second parentheses) represent F_e for illumination by s polarization. On the other hand, F_m is the magnetic component of F . The first term denotes the interactions between two m_x while the second one is the force exerted on m_x^B by p_z^A . The first two

terms (in the first parentheses) represent F_m in the case of p polarization. The third and fourth terms denote respectively the interactions between two m_y and between two m_z . The last term shows the force exerted on m_z^B by p_x^A . The last three terms (in the second parentheses) determine F_m for s polarization. Finally, F_{em} is the electric-magnetic coupling component of F . The first term comes from the interference between p_z^B and m_x^A and represents F_{em} for p polarization. The last term originates from the interference between p_x^B and m_z^A and represents F_{em} in the case of s polarization.

For Rayleigh particles ($\alpha_m = 0$) whose refractive index or radius is small enough to satisfy the relation $kr = 2\pi n_p r/\lambda \ll 1$, F is determined by only the first and fifth terms in Eq. (1) while $F_m = F_{em} = 0$. In this case, the force is the classical optical binding force (F_{Ray}) between two electric dipolar particles, the same as Eq. (3a) in Ref. [15]. On the other hand, for magnetic dipolar particles ($\alpha_e = 0$) such as Au core-Si shell nanospheres [31], the only nonzero contributions to F are the first and third terms in Eq. (2), which together constitute the magnetic binding force [32], while $F_e = F_{em} = 0$.

In addition to the binding force, the incident light also causes an extrinsic optical torque (Γ) on the dimer [15] which causes the dimer to rotate around the z axis. The torque is also composed of three parts:

$$\Gamma_e = \frac{\varepsilon_0 \varepsilon_s}{2} \left\{ \begin{aligned} & 2\text{Re}[\kappa - \mu] \text{Re}[\tilde{\alpha}_{em-s,2} \tilde{\alpha}_{ey}^* E_{0,x} E_{0,y}^*] \\ & + \text{Re}[\eta(\tilde{\alpha}_{my} \tilde{\alpha}_{em-p,1}^* - \tilde{\alpha}_{em-s,1} \tilde{\alpha}_{ey}^*) E_{0,x} E_{0,y}^*] \end{aligned} \right\}, \quad (4)$$

$$\Gamma_m = \frac{\varepsilon_0 \varepsilon_s}{2} \left\{ \begin{aligned} & -2\text{Re}[\kappa - \mu] \text{Re}[\tilde{\alpha}_{em-p,2} \tilde{\alpha}_{my}^* E_{0,x} E_{0,y}^*] \\ & + \text{Re}[\eta(\tilde{\alpha}_{em-p,1} \tilde{\alpha}_{my}^* - \tilde{\alpha}_{ey} \tilde{\alpha}_{em-s,1}^*) E_{0,x} E_{0,y}^*] \end{aligned} \right\}, \quad (5)$$

$$\Gamma_{em} = \frac{\varepsilon_0 \varepsilon_s k^4 R}{12\pi} \text{Im}[(\tilde{\alpha}_{ey} \tilde{\alpha}_{em-s,1}^* + \tilde{\alpha}_{em-p,1} \tilde{\alpha}_{my}^*) E_{0,x}^* E_{0,y}]. \quad (6)$$

Γ_e is the electric component of Γ . The first term denotes the interaction of p_x^B with p_y^A and the interaction of p_y^B with p_x^A . The last two terms (in the last square brackets) indicate respectively the interaction of p_z^B with m_y^A and the interaction of p_y^B with m_z^A . In addition, Γ_m is the magnetic component of Γ . The first term represents the interaction of m_x^B with m_y^A and interaction of m_y^B with m_x^A . The last two (in the last square brackets) represent respectively the interaction of m_y^B with p_z^A and interaction of m_z^B with p_y^A . Moreover, Γ_m is the electric-magnetic coupling component of Γ . The first term originates from the interference between p_y^B and m_z^B while the second one comes from the interference between p_z^B and m_y^B .

For Rayleigh particles, Γ_e is determined by only the first term in Eq. (4) while $\tilde{\alpha}_{em-s,2}$ reduces to $\tilde{\alpha}_{ex}$. This agrees with the classical torque on a Rayleigh-approximation dimer [15]. Meanwhile $\Gamma_m = \Gamma_{em} = 0$. On the other hand, for purely magnetic dipolar particles, Γ_m is determined only by the first term in Eq. (5) and $\tilde{\alpha}_{em-p,2}$ is simplified to $\tilde{\alpha}_{mx}$, in agreement with magnetic optical torque between two magnetic dipolar particles in [32]. In this case, $\Gamma_m = \Gamma_{em} = 0$. Note that for p and s polarizations the torque vanishes. Equations (1)–(6) are general for a plane wave in the near field, intermediate field, and far field. They are the main results in this paper. Our numerical calculations are based on Eqs. (1)–(6).

Furthermore, the force and torque can be simplified in the far-field region ($kR \gg 1$) where we retain only the highest order terms of kR in μ , κ , and η . For p polarization, Eqs. (1)–(3) are respectively simplified as

$$F_e = \frac{n_s I_0}{c} \left\{ \frac{k^2 |\alpha_e|^2}{2\pi R^2} \cos(kR) + \frac{k^5 |\alpha_m|^2}{(4\pi R)^2} \text{Im}[\alpha_e] \right\}, \quad (7)$$

$$F_m = -\frac{n_s I_0 k^3 |\alpha_m|^2}{c} \sin(kR), \quad (8)$$

$$F_{em} = \frac{n_s I_0 k^6 |\alpha_m|^2}{c} \frac{1}{24\pi^2 R} \{ \cos(kR) \text{Re}[\alpha_e] - \sin(kR) \text{Im}[\alpha_e] \}, \quad (9)$$

where $I_0 = \varepsilon_0 n_s c |E_0|^2 / 2$ is the intensity of the incident wave in the medium, c is light speed in vacuum, E_0 is the amplitude of the incident electric field, $\alpha_e = i6\pi a_1 / k^3$, and $\alpha_m = i6\pi b_1 / k^3$ are the electric and magnetic polarizabilities with radiation reaction terms of the particles where a_1 and b_1 are respectively the electric and magnetic dipolar Mie scattering coefficients [33], and i is the unit imaginary number. Equations (7)–(9) demonstrate that F_e is proportional to R^{-2} as shown by the red short dashed curve in Fig. 2(a) while F_m and F_{em} are proportional to R^{-1} as shown by the blue dash-dotted and green dash-dot-dotted curves. The results indicate that F_e decays faster than F_m and F_{em} in the far field. For Rayleigh particles, the binding force is completely determined by the first term in Eq. (7), which is in agreement with Ref. [34]. On the other hand for a purely magnetic dipolar dimer, the binding force is completely determined by Eq. (8). In the case of s polarization, F_e is expressed by Eq. (8) by replacing

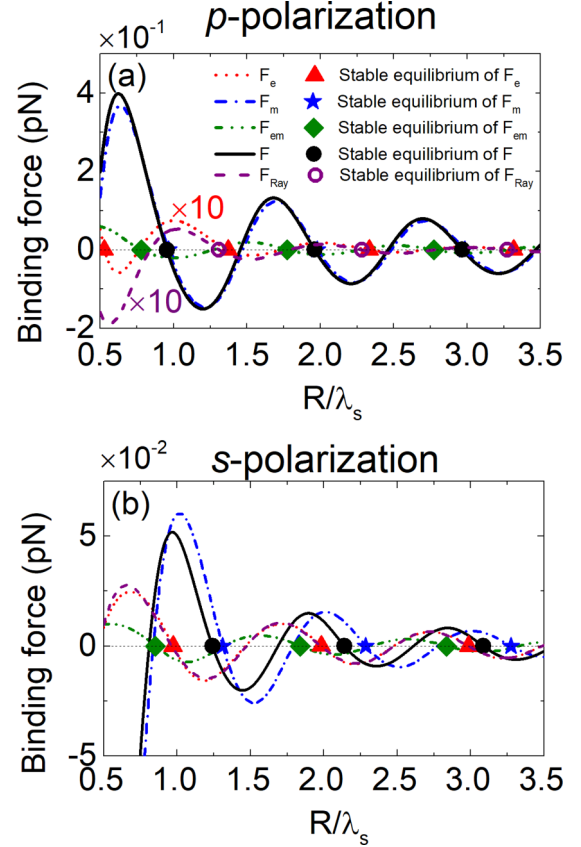


FIG. 2. Binding force vs distance (R) between the centers of two spheres ($r = 100$ nm and $n_p = 4$) for p polarization (a) and s polarization (b). F (black solid curve) is the binding force while F_e (red short dashed curve), F_m (blue dash-dotted curve), and F_{em} (green dash-dot-dotted curve) are respectively the electric, magnetic, and coupling components of F . F_{Ray} (purple dashed curve) is the binding force in the Rayleigh approximation. The digits in (a) indicate a multiple of the magnified forces. The triangles, stars, diamonds, circles, and hollow circles represent respectively the stable equilibrium positions of F_e , F_m , F_{em} , F , and F_{Ray} .

α_m with α_e , which is the binding force in the Rayleigh approximation. F_m and F_{em} are respectively written as Eqs. (7) and (9) by exchanging α_m and α_e . Therefore, $F_m \propto R^{-2}$ as shown by the blue dash-dotted curve in Fig. 2(b) while F_e and $F_{em} \propto R^{-1}$ as shown by the red short dashed and green dash-dot-dotted curves. It means F_m decays faster than F_e and F_{em} . The first term in F_m represents the binding force between two pure magnetic dipolar particles. Finally, for left-hand circular polarization with $\mathbf{e}_0 = E_0(1, i, 0) \exp(ikz) / \sqrt{2}$ [35], F_e and F_m are expressed by Eq. (8) through employing respectively α_e and α_m . In this case, $F_e = F_{Ray}$ and F_m is the binding force between two magnetic dipolar particles. Moreover, the coupling component of the binding force is read as

$$F_{em} = \frac{n_s I_0}{c} \frac{k^6}{48\pi^2 R} \times \left\{ \begin{array}{l} \cos(kR) (|\alpha_m|^2 \text{Re}[\alpha_e] + |\alpha_e|^2 \text{Re}[\alpha_m]) \\ - \sin(kR) (|\alpha_m|^2 \text{Im}[\alpha_e] + |\alpha_e|^2 \text{Im}[\alpha_m]) \end{array} \right\}. \quad (10)$$

The above results show that the binding force $F \propto R^{-1}$. Additionally, the electric component of torque is read as

$$\Gamma_e = \frac{n_s I_0}{2c} \frac{k^4}{(4\pi R)^2} \left\{ \begin{array}{l} (|\alpha_e|^2 + |\alpha_m|^2) \text{Im}[\alpha_e] \\ -|\alpha_e|^2 \left(\begin{array}{l} \cos(2kR) \text{Im}[\alpha_m - \alpha_e] \\ + \sin(2kR) \text{Re}[\alpha_m - \alpha_e] \end{array} \right) \end{array} \right\}. \quad (11)$$

The magnetic component of torque Γ_m is also expressed by Eq. (11) through exchanging α_e and α_m . Moreover, the coupling component of torque Γ_{em} is written as

$$\Gamma_{em} = \frac{n_s I_0}{2c} \frac{k^6}{24\pi^2} \left\{ \begin{array}{l} \cos(kR) (|\alpha_e|^2 \text{Im}[\alpha_m] + |\alpha_m|^2 \text{Im}[\alpha_e]) \\ + \sin(kR) (|\alpha_e|^2 \text{Re}[\alpha_m] + |\alpha_m|^2 \text{Re}[\alpha_e]) \end{array} \right\}. \quad (12)$$

Notice that Γ_e and Γ_m while, interestingly, Γ_{em} is independent of R . Therefore, the torque is dominated by the coupling interaction, which is completely different than the binding force. Furthermore, the torque in the Rayleigh approximation ($\alpha_m = 0$) is simplified from Eq. (11) as

$$\Gamma_{\text{Ray}} = \frac{n_s I_0}{2c} \frac{k^4 |\alpha_e|^2}{(4\pi R)^2} \{ [\cos(2kR) + 1] \text{Im}[\alpha_e] + \sin(2kR) \text{Re}[\alpha_e] \}. \quad (13)$$

On the other hand, for a purely magnetic dipolar dimer, the torque Γ_{MD} is also expressed by Eq. (13) through replacing α_e by α_m . Notice that we focus on the optical binding between dual dipolar particles without considering the electric quadrupole-assisted force. This is because the electric quadrupole is not dominant compared to the dipolar resonances within our parameters.

III. RESULTS AND DISCUSSION

A. TOBFs for p - and s -polarized waves

We consider two spheres with high refractive index $n_p = 4$, i.e., germanium [36], immersed in water ($n_s = 1.33$) (a discussion of the forces and torques on particles with lower refractive index is given in Appendixes G–L). The wavelengths of the incident wave in vacuum and water are $\lambda_0 = 532$ nm and $\lambda_s = \lambda_0/n_s = 400$ nm, respectively. The power density of the wave in water is $I_0 = 10$ mW/ μm^2 . To demonstrate the applicability of our model beyond the Rayleigh regime, we model spheres of radius $r = 100$ or 150 nm. As expected, in the small r limit, our model will degenerate to the Rayleigh approximation, as discussed in Eqs. (1)–(6). The force, torque, and distance (R) are respectively in units of pN, pN μm , and λ_s .

Figure 2 shows F (black solid curve) as well as F_e (red short dashed curve), F_m (blue dash-dotted curve), and F_{em} (green dash-dot-dotted curve) between dielectric particles with $r = 100$ nm and $n_p = 4$ as a function of the distance R between the centers of the two particles for (a) p -polarized and (b) s -polarized waves. Additionally, F_{Ray} (purple dashed curve) is presented as a comparison. It can be seen from Fig. 2(a) that in the case of p polarization F_m greatly exceeds F_e and F_{em} and dominates F . Physically, the effects of hybridization are particularly pronounced for high-refractive-index particles. For example, the reradiated field by m_x in one particle is strong

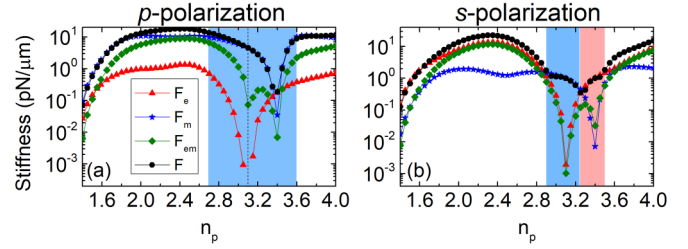


FIG. 3. The stiffness at the first stable equilibrium positions of F , F_e , F_m , and F_{em} versus refractive index (n_p) of particles with $r = 150$ nm for p polarization (a) and s polarization (b). The faint blue shaded area where $2.7 < n_p < 3.6$ in (a) denotes the region where the stiffness of F is dominated by that of F_m . The vertical black dashed line marks the location $n_p = 3.1$. The faint blue ($2.9 < n_p < 3.24$) and red ($3.24 < n_p < 3.5$) shaded areas in (b) represent the regions where the stiffness of F is respectively dominated by those of F_m and F_e .

enough to induce p_z in the neighboring one. Thus F_e does not only depend on the interaction between p_y^A and p_y^B , which is the case for Rayleigh particles, but also by the interactions between m_x^A and p_z^B and between p_z^A and p_z^B . Previous theoretical work demonstrated that the magnetic TOBF of an ideal magnetic dimer can be enhanced to the same magnitude as the TOBF for Rayleigh particles [32]. But what is surprising here is that the F_m is an order of magnitude larger than not only F_{Ray} but also F_e . The reason is that the p_y induced in the two particles by the incident wave is nearly suppressed at wavelength $\lambda_0 = 532$ nm while the two m_x are excited even though they do not reach the maximum resonance (see Figs. 2 and 3 in Ref. [37]). As a result, F is dominated by contributions from F_m while the stable equilibrium positions of F (black circles) are determined by those of F_m (blue stars) instead of those of F_e (red triangles) and F_{em} (blue diamonds). The results demonstrate that F_{Ray} dramatically underestimates F for dielectric particles with high refractive index. Similar phenomena are observed in s polarization in Fig. 2(b). With increasing refractive index, the relative contribution of F_e to the binding force is gradually overtaken by that due to F_m (see details in Appendixes H and I). However, we emphasize that even for low-refractive-index particles such as polystyrene ($n_p = 1.59$), non-negligible components of F_m and F_{em} already arise, and the magnitudes of these exceed the magnitude of F_e for moderate refractive indices such as silicon ($n_p = 3.5$) in p polarization (see details in Appendixes G and H). Additionally, F in the case of p polarization is larger than that for s polarization. The reasons are that the interaction between two side-by-side parallel m_x in p polarization is larger than that between two head-to-tail collinear m_y in s polarization, while the electric dipolar interactions are suppressed.

Moreover, we calculated the first stable equilibrium positions of F , F_e , F_m , and F_{em} (see details in Appendix I) as well as the stiffness at these positions for dielectric particles with n_p from 1.4 to 4 in cases of p and s polarizations in Fig. 3. Within this range, many materials of interest in optical trapping are concentrated, e.g., polystyrene ($n_p = 1.59$) [38], diamond ($n_p = 2.4$) [39], silicon ($n_p = 3.5$) [40], bismuth ($n_p = 3.89$) [28], and germanium ($n_p = 4$) [26]. The particle's radius is set to 150 nm in order to improve further its magnetic

response because the magnetic dipole moment caused by the displacement current in the particle increases with the particle size. In detail, for p polarization in Fig. 3(a), the stiffness of F_e (red curve with triangles) decreases sharply in the blue shaded region $2.7 < n_p < 3.6$, meaning that F_e is barely sufficient for the formation of a stable bound state. The stable equilibrium vanishes completely at $n_p = 3.1$ (vertical black dashed line) where F_e has no stiffness and formation of a stable dimer is prohibited (see details in Appendix J). On the other hand, the stiffness of F_m (blue curve with stars) is much larger than those of F_{em} (green curve with diamonds) and F_e . Notably, for particles with n_p from 2.7 to 3.6, the stiffness of F_e decreases rapidly and even vanishes, because the suppressed electric dipolar responses cause the electric dipole-dipole interaction to provide barely sufficient potential well depths to bind the two particles. However, the stiffness of F_m is one to four orders of magnitude larger than that of F_e . Surprisingly, out of this region, the stiffness of F_m is still one order of magnitude larger than that of F_e . This means that F (black curve with circles) is mainly dominated by F_m , which shows the predominant ability of F_m to bind the dielectric dimer for p polarization. For s polarization in Fig. 3(b), the stiffness of F_e and F_{em} are of the same order of magnitude and much larger than that of F_m . Interestingly, in the region $2.9 < n_p < 3.24$ (faint blue area), the stability of the dimer is dominated by F_m , but in the neighboring region $3.24 < n_p < 3.5$ (faint red area), the stability is dominated by F_e . Therefore, F_e and F_m supplement each other to enable stable formation of the dimer. It can be clearly seen from Fig. 3 that the magnetic dipolar interaction dominates the stability of the dimer in p polarization while the electric dipolar interaction is dominant in s polarization.

B. TOBF and torque for circularly polarized waves

Figure 4(a) shows F , F_e , F_m , and F_{em} for left-hand circular polarization for the same parameters as in Fig. 2. The electric dipoles are again greatly suppressed compared to the magnetic dipoles and F_m provides the leading contribution to F . As a result, the stable equilibrium positions of F are very close to the counterparts of F_m (not marked). This is similar to the p - and s -polarized cases in Fig. 2. Figure 4(b) shows that the radial (along the dimer's axis) stability (stiffness) of the dimer at the first radial stable equilibrium position (see details in Appendix K) is determined by different components of F . In the low-refractive-index region (left faint red area $1.4 < n_p < 1.59$) the stability is determined by F_e . With increase of n_p , the stability is controlled by all components of F . Interestingly in the middle-refractive-index region (faint blue area $2.9 < n_p < 3.25$) F_m provides robust stability where the stiffness of F_e and F_{em} drops sharply. On the contrary, F_e sustains the stability where the stiffness of F_m and F_{em} reduces sharply (right faint red area $3.25 < n_p < 3.45$). Hence, F_e and F_m supplement each other in the radial stability of the dimer which is similar to the s polarization in Fig. 3(b).

Under circularly polarized light, a dimer experiences not only a radial force due to the TOBF, but is also subjected to a torque about the center of mass. Figure 4(c) shows the torque (Γ) and its components Γ_e , Γ_m , and Γ_{em} as functions of R . The envelopes of Γ_e and Γ_m decay $\propto R^{-1}$ as shown by Eq. (11). Interestingly, the envelope of Γ_{em} is independent of

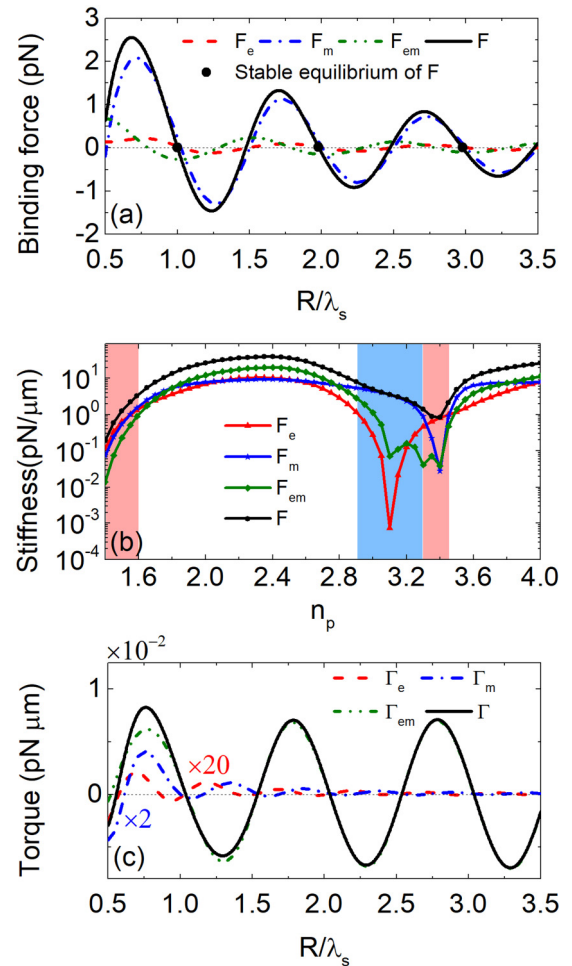


FIG. 4. Optical binding for left-circular polarization. (a) Binding force F including F_e , F_m , and F_{em} vs distance R . The black circles denote the stable equilibrium positions of F . (b) The stiffness at the first stable equilibrium positions of F_e , F_m , F_{em} , and F vs n_p . The faint blue ($2.9 < n_p < 3.25$) and red ($1.4 < n_p < 1.59$ and $3.25 < n_p < 3.45$) shaded areas in (b) show the regions where the stiffness of F is respectively dominated by those of F_m and F_e . (c) Torque Γ including Γ_e , Γ_m , and Γ_{em} vs distance R . The digits in (c) indicate a multiple of the magnified torques. The parameters in (a) and (c) are the same as in Fig. 2. The parameters in (b) are the same as in Fig. 3.

R [as shown by Eq. (12)] which is similar to magnetodielectric particles [24]. Hence, Γ_{em} plays the leading role in Γ , which is completely different than the binding force (see details in Appendix L).

As expected, when the polarization is changed from left- to right-handed circular, the binding force stays the same but the torque in Fig. 4(c) changes sign.

IV. CONCLUSIONS

In summary, we have presented analytical solutions for the TOBF and torque on two identical dual dipolar dielectric particles in a plane EM wave. The electric and the magnetic dipolar interactions dominate the force in different regimes of refractive index, while the torque experienced by the dimer in circularly polarized light is always dominated by

the electric-magnetic coupling interaction. This shows that all three components must be considered for an accurate understanding of the stability and dynamics of dimers formed from high refractive index particles. Furthermore, the force, torque, and stability of the dimer with high refractive index are significantly enhanced by both magnetic and coupling interactions. The conclusions demonstrate clearly that the force, torque, and stability of the particles may be underestimated to a high degree if one uses the Rayleigh approximation. Our results have potential applications in light-controlled self-assembly of dielectric materials of high refractive index. Visualizing these key differences between the different regimes of refractive index would be intriguing in an experimental optical binding geometry. We note that in typical experiments the dimer is suspended in liquid medium and subjected to optical and random forces. For a quantitative agreement between experiment and the results presented here, it may therefore be necessary to enforce a stable transverse configuration between the dimer and incident beam, e.g., by using a standing-wave optical trap [41,42]. In addition to the accurate determination of particle positions of the dimers there are also prospects for observing the interparticle field directly using multiphoton excitation of the medium in which the particles are suspended [43].

ACKNOWLEDGMENTS

This work was supported by the National Key R&D Program of China (Grant No. 2017YFA0303400) and the Postgraduate Education Reform Project of Tongji University (Grant No. 2018GH103). K.D. acknowledges support of the UK Engineering and Physical Sciences Research Council (Grant No. EP/P030017/1).

APPENDIX A: CALCULATION OF OPTICAL FORCE

It is assumed that a dimer consisting of two identical dielectric nanospheres is immersed in water and illuminated by an arbitrarily polarized plane EM wave. The configuration is shown by Fig. 1 in the main text. The total field encircling one particle is the sum of the incident field and the field scattered by the neighboring particle. For instance, taking into account the mutual scattering between particles, the total electric (\mathbf{E}^B) and magnetic (\mathbf{H}^B) fields surrounding particle B are expressed as [30]

$$\mathbf{E}^B = \mathbf{E}_0^B + \frac{1}{\varepsilon_0 \varepsilon_s} \vec{\mathbf{G}}_e(\mathbf{r}_B - \mathbf{r}_A) \cdot \mathbf{p}^A + iZ \vec{\mathbf{G}}_m(\mathbf{r}_B - \mathbf{r}_A) \cdot \mathbf{m}^A, \quad (\text{A1})$$

$$\mathbf{H}^B = \mathbf{H}_0^B - \frac{i}{Z \varepsilon_0 \varepsilon_s} \vec{\mathbf{G}}_m(\mathbf{r}_B - \mathbf{r}_A) \cdot \mathbf{p}^A + \vec{\mathbf{G}}_e(\mathbf{r}_B - \mathbf{r}_A) \cdot \mathbf{m}^A, \quad (\text{A2})$$

where \mathbf{r}_A and \mathbf{r}_B are positions of the centers of the two particles and $Z = [\mu_0 \mu_s / (\varepsilon_0 \varepsilon_s)]^{1/2}$ is the impedance of the medium. $\mathbf{p}^A = \varepsilon_0 \varepsilon_s \alpha_e \mathbf{E}^A$ and $\mathbf{m}^A = \alpha_m \mathbf{H}^A$ represent respectively the electric and magnetic dipole moments in particle A induced by the total electric (\mathbf{E}^A) and magnetic (\mathbf{H}^A) fields at particle A (the expressions for \mathbf{p} and \mathbf{m} in particle B are obtained by substituting the letter A by B).

$\vec{\mathbf{G}}_e(\mathbf{r}_B - \mathbf{r}_A)$ and $\vec{\mathbf{G}}_m(\mathbf{r}_B - \mathbf{r}_A)$ are free-space electric and magnetic dyadic Green's functions of a point dipole [44] (see details in Appendix B). The first term in Eq. (A1) [Eq. (A2)] represents the incident electric (magnetic) field at particle B , the second one denotes the scattered electric (magnetic) field on particle B by the electric dipole in particle A , and the last term expresses the scattered electric (magnetic) field on particle B by the magnetic dipole in particle A . Additionally, the total electric and magnetic fields in the nearby particle A are also described by Eqs. (A1) and (A2) through interchanging the superscripts B and A while considering the relations $\vec{\mathbf{G}}_e(\mathbf{r}_B - \mathbf{r}_A) = \vec{\mathbf{G}}_e(\mathbf{r}_A - \mathbf{r}_B)$ and $\vec{\mathbf{G}}_m(\mathbf{r}_A - \mathbf{r}_B) = -\vec{\mathbf{G}}_m(\mathbf{r}_B - \mathbf{r}_A)$. Hereafter we simplify the notation $\vec{\mathbf{G}}_e(\mathbf{r}_B - \mathbf{r}_A) \equiv \vec{\mathbf{G}}_e$ and $\vec{\mathbf{G}}_m(\mathbf{r}_B - \mathbf{r}_A) \equiv \vec{\mathbf{G}}_m$ for convenience. By decomposing vector Eqs. (A1) and (A2) into scalar equations along the three axes and solving them for particles A and B in terms of μ , κ , and η , the x , y , and z components of the electric and magnetic dipole moments in each particle are derived in Eqs. (A7)–(A12).

It is convenient to define dressed polarizabilities to describe the polarization of the particles under the incoming waves. In detail, the electric dressed polarizabilities are described by

$$\tilde{\alpha}_{ex} = \frac{\alpha_e}{1 - \alpha_e \mu}, \quad \tilde{\alpha}_{ey} = \frac{\alpha_e}{1 - \alpha_e \kappa}, \quad \tilde{\alpha}_{ez} = \frac{\alpha_e}{1 + \alpha_e \mu}, \quad (\text{A3})$$

where $\tilde{\alpha}_{e\nu}$ ($\nu = x, y, \text{ and } z$) is caused by the hybridization of two ν components of the electric dipole moments (p_ν) in different particles. On the other hand, the magnetic dressed polarizabilities are expressed as

$$\tilde{\alpha}_{mx} = \frac{\alpha_m}{1 - \alpha_m \mu}, \quad \tilde{\alpha}_{my} = \frac{\alpha_m}{1 - \alpha_m \kappa}, \quad \tilde{\alpha}_{mz} = \frac{\alpha_m}{1 + \alpha_m \mu}, \quad (\text{A4})$$

where $\tilde{\alpha}_{m\nu}$ is the result of hybridization between ν components of the magnetic dipole moments (m_ν) in two particles. In addition, the p -polarized dressed polarizabilities are given by

$$\tilde{\alpha}_{em-p,1} = \frac{\tilde{\alpha}_{ez} \tilde{\alpha}_{mx} \eta}{1 - \tilde{\alpha}_{ez} \tilde{\alpha}_{mx} \eta^2}, \quad \tilde{\alpha}_{em-p,2} = \frac{\tilde{\alpha}_{mx}}{1 - \tilde{\alpha}_{ez} \tilde{\alpha}_{mx} \eta^2}, \quad (\text{A5})$$

where $\tilde{\alpha}_{em-p,1}$ originates from the hybridization of p_z in one particle with p_z and m_x in another while $\tilde{\alpha}_{em-p,2}$ is a result of the hybridization of m_x in one particle with m_x and p_z in the other one. They can be thought of as being induced by the p -polarized wave (\mathbf{H}_0 is perpendicular to the incident plane and along the x axis) which causes the m_x in the two particles. Moreover, the s -polarized dressed polarizabilities are written as

$$\tilde{\alpha}_{em-s,1} = \frac{\tilde{\alpha}_{ex} \tilde{\alpha}_{mz} \eta}{1 - \tilde{\alpha}_{ex} \tilde{\alpha}_{mz} \eta^2}, \quad \tilde{\alpha}_{em-s,2} = \frac{\tilde{\alpha}_{ex}}{1 - \tilde{\alpha}_{ex} \tilde{\alpha}_{mz} \eta^2}, \quad (\text{A6})$$

where $\tilde{\alpha}_{em-s,1}$ comes from the hybridization of m_z in one particle with m_z and p_x in the other, while $\tilde{\alpha}_{em-s,2}$ stems from the hybridization of p_x in one particle with p_x and m_z in the neighboring one. They can be regarded as a result of the s -polarized wave (\mathbf{E}_0 is perpendicular to the incident plane and along the x axis) which induces the p_x in the two particles.

The self-consistent electric and magnetic dipole moments in the two particles induced by an arbitrarily polarized EM wave and hybridization between the particles are expressed as

$$p_x^A = p_x^B = \varepsilon_0 \varepsilon_s \tilde{\alpha}_{\text{em}-s,2} E_{0,x}, \quad (\text{A7})$$

$$p_y^A = p_y^B = \varepsilon_0 \varepsilon_s \tilde{\alpha}_{\text{ey}} E_{0,y}, \quad (\text{A8})$$

$$p_z^A = -p_z^B = i \varepsilon_0 \varepsilon_s \tilde{\alpha}_{\text{em}-p,1} E_{0,y}, \quad (\text{A9})$$

$$m_x^A = m_x^B = \tilde{\alpha}_{\text{em}-p,2} H_{0,x}, \quad (\text{A10})$$

$$m_y^A = m_y^B = \tilde{\alpha}_{\text{my}} H_{0,y}, \quad (\text{A11})$$

$$m_z^A = -m_z^B = i \tilde{\alpha}_{\text{em}-s,1} H_{0,y}. \quad (\text{A12})$$

Equation (A7) denotes that p_x in one particle is partly excited by the incident electric field $E_{0,x}$ and partly hybridized by both p_x and m_z in the neighboring particle. Equation (A8) indicates that p_y in one particle is hybridized by p_y in the other in addition to the induction by the incident electric field $E_{0,y}$. Equation (A9) shows that p_z in one particle is hybridized by both p_z and m_x in the other particle, rather than by the induction of the incident electric field. Equation (A10) reveals that m_x in one particle is not only induced by the incident magnetic field $H_{0,x}$ but also hybridized by both p_z and m_x in the other particle. Equation (A11) exhibits that m_y in one particle is caused by the incident magnetic field $H_{0,y}$ and hybridized by m_y in the neighboring particle. Equation (A12) denotes that m_z in one particle is hybridized by both p_x and m_z in the neighboring particle and independent of the incident magnetic field (see details in Appendix C). For a p -polarized wave, $\tilde{\alpha}_{\text{my}}$, $\tilde{\alpha}_{\text{mz}}$, $\tilde{\alpha}_{\text{ex}}$, $\tilde{\alpha}_{\text{em}-s,1}$, and $\tilde{\alpha}_{\text{em}-s,2}$ disappear as well as $p_x^{A(B)} = m_y^{A(B)} = m_z^{A(B)} = 0$ due to the absence of $E_{0,x}$ and $H_{0,y}$. On the other hand, for s polarization without $E_{0,y}$ and $H_{0,x}$, the $\tilde{\alpha}_{\text{mx}}$, $\tilde{\alpha}_{\text{ey}}$, $\tilde{\alpha}_{\text{ez}}$, $\tilde{\alpha}_{\text{em}-p,1}$, and $\tilde{\alpha}_{\text{em}-p,2}$ vanish while $p_y^{A(B)} = p_z^{A(B)} = m_x^{A(B)} = 0$.

For calculation of the optical force, taking particle B as an example, the spatial derivatives of the total electric and magnetic fields at particle B are solved as

$$\frac{\partial \mathbf{E}^B}{\partial u} = \frac{\partial \mathbf{E}_0^B}{\partial u} + \frac{1}{\varepsilon_0 \varepsilon_s} \frac{\partial \tilde{\mathbf{G}}_e}{\partial u} \cdot \mathbf{p}^A + iZ \frac{\partial \tilde{\mathbf{G}}_m}{\partial u} \cdot \mathbf{m}^A, \quad (\text{A13})$$

$$\frac{\partial \mathbf{H}^B}{\partial u} = \frac{\partial \mathbf{H}_0^B}{\partial u} - \frac{i}{Z \varepsilon_0 \varepsilon_s} \frac{\partial \tilde{\mathbf{G}}_m}{\partial u} \cdot \mathbf{p}^A + \frac{\partial \tilde{\mathbf{G}}_e}{\partial u} \cdot \mathbf{m}^A, \quad (\text{A14})$$

where $\partial/\partial u$ denotes the partial derivative with respect to the arguments x and y . The partial derivatives of the located fields \mathbf{E} and \mathbf{H} at particle A also can be calculated by Eqs. (A13) and (A14) through exchanging the letters A and B while considering the relations $\partial \tilde{\mathbf{G}}_e/\partial u|_A = -\partial \tilde{\mathbf{G}}_e/\partial u|_B$ and $\partial \tilde{\mathbf{G}}_m/\partial u|_A = \partial \tilde{\mathbf{G}}_m/\partial u|_B$. The matrix forms of $\tilde{\mathbf{G}}_{e(m)}$ and $\partial \tilde{\mathbf{G}}_{e(m)}/\partial u$ and the scalar decompositions of Eqs. (A13) and (A14) are presented in Appendixes D and E. The time-averaged optical force on a dielectric particle with induced electric and magnetic dipoles

is given by [29]

$$\mathbf{F} = \frac{1}{2} \text{Re} \left[(\mathbf{p} \nabla) \mathbf{E}^* + \mu_0 \mu_s (\mathbf{m} \nabla) \mathbf{H}^* - \frac{Zk^4}{6\pi} (\mathbf{p} \times \mathbf{m}^*) \right]. \quad (\text{A15})$$

The first two terms on the right-hand side of Eq. (A15) are respectively the forces on the electric and magnetic dipoles while the last one is the electric-magnetic coupling force due to the interference between the two dipoles.

APPENDIX B: EIGENVALUES OF $\tilde{\mathbf{G}}_e$ AND $\tilde{\mathbf{G}}_m$

The free-space electric ($\tilde{\mathbf{G}}_e$) and magnetic ($\tilde{\mathbf{G}}_m$) dyadic Green's functions are written as [44]

$$\tilde{\mathbf{G}}_e = \frac{\exp(ikR)}{4\pi R^3} \left[(3 - 3ikR - k^2 R^2) \frac{\mathbf{R}\mathbf{R}}{R^2} + (-1 + ikR + k^2 R^2) \tilde{\mathbf{I}} \right], \quad (\text{B1})$$

$$\tilde{\mathbf{G}}_m = \frac{\exp(ikR)}{4\pi R^3} (ik^2 R^2 - kR) \frac{\mathbf{R} \times \tilde{\mathbf{I}}}{R}, \quad (\text{B2})$$

where $\tilde{\mathbf{I}}$ is the unit dyad. Equation (B2) is derived from Eq. (B1) by utilizing the orthogonality relation $\tilde{\mathbf{G}}_m = (\nabla \times \tilde{\mathbf{G}}_e)/k$. For simplified calculations of the induced dipole moments in particles and TOBF, $\tilde{\mathbf{G}}_e$ is expressed in terms of the eigenequation [22] as

$$\tilde{\mathbf{G}}_e = (\kappa - \mu) \frac{\mathbf{R}\mathbf{R}}{R^2} + \mu \tilde{\mathbf{I}}, \quad (\text{B3})$$

where the eigenvalues κ and μ of $\tilde{\mathbf{G}}_e$ are determined by

$$\mu = \frac{\exp(ikR)}{4\pi R^3} (k^2 R^2 + ikR - 1), \quad (\text{B4})$$

$$\kappa = \frac{\exp(ikR)}{4\pi R^3} (-2ikR + 2). \quad (\text{B5})$$

Since any vector \mathbf{V} can be decomposed into two components \mathbf{V}_{\parallel} and \mathbf{V}_{\perp} who are respectively parallel and perpendicular to vector \mathbf{R} , based on Eq. (B3), the dot product between $\tilde{\mathbf{G}}_e$ and any vector \mathbf{V} is given by

$$\tilde{\mathbf{G}}_e \cdot \mathbf{V} = \kappa \mathbf{V}_{\parallel} + \mu \mathbf{V}_{\perp}, \quad (\text{B6})$$

which denotes that the eigenvectors of κ and μ are respectively parallel and orthogonal to vector \mathbf{R} . Then, we have

$$\tilde{\mathbf{G}}_e \cdot (\mathbf{e}_x, \mathbf{e}_y, \mathbf{e}_z) = (\mu \mathbf{e}_x, \kappa \mathbf{e}_y, \mu \mathbf{e}_z), \quad (\text{B7})$$

where \mathbf{e}_x , \mathbf{e}_y , and \mathbf{e}_z are unit vectors along x , y , and z axes in the Cartesian system. On the other hand, the eigenequation of $\tilde{\mathbf{G}}_m$ is written as

$$\tilde{\mathbf{G}}_m = \eta \mathbf{R} \times \tilde{\mathbf{I}}/R, \quad (\text{B8})$$

where the eigenvalue η of $\tilde{\mathbf{G}}_m$ is expressed as

$$\eta = \frac{\exp(ikR)}{4\pi R^3} (ik^2 R^2 - kR). \quad (\text{B9})$$

Equation (B8) demonstrates that the eigenvector of η is orthogonal to vector \mathbf{R} . Analogous to Eq. (B6), based on

Eq. (B8), the dot product between $\vec{\mathbf{G}}_m$ and any vector \mathbf{V} is expressed by

$$\vec{\mathbf{G}}_m \cdot \mathbf{V} = \eta \mathbf{V}_\perp. \quad (\text{B10})$$

Hence, the dot product between $\vec{\mathbf{G}}_m$ and unit vectors is expressed as

$$\vec{\mathbf{G}}_m \cdot (\mathbf{e}_x, \mathbf{e}_y, \mathbf{e}_z) = (-\eta \mathbf{e}_z, 0, \eta \mathbf{e}_x). \quad (\text{B11})$$

APPENDIX C: INDUCED DIPOLE MOMENTS IN DIMER

By substituting Eqs. (B7) and (B11) into Eq. (A1), the three components of the total electric field on particle A (B) are expressed by

$$E_x^{A(B)} = E_{0,x}^{A(B)} + \frac{1}{\varepsilon_0 \varepsilon_s} \mu p_x^{B(A)} \mp i Z \eta m_z^{B(A)}, \quad (\text{C1})$$

$$E_y^{A(B)} = E_{0,y}^{A(B)} + \frac{1}{\varepsilon_0 \varepsilon_s} \kappa p_y^{B(A)}, \quad (\text{C2})$$

$$E_z^{A(B)} = \frac{1}{\varepsilon_0 \varepsilon_s} \mu p_z^{B(A)} \pm i Z \eta m_x^{B(A)}. \quad (\text{C3})$$

Notice that for electric field on particle A , the signs of the third term in Eq. (C1) and the second term in Eq. (C3) are respectively negative and positive while they are opposite for particle B . The regulations of the signs are also appropriate for the following Eqs. (C4) and (C6). Considering the relation $\mathbf{p} = \varepsilon_0 \varepsilon_s \alpha_e \mathbf{E}$, the three components of the electric dipole moment in particle A (B) are given by

$$p_x^{A(B)} = \varepsilon_0 \varepsilon_m \alpha_e E_{0,x}^{A(B)} + \alpha_e \mu p_x^{B(A)} \mp i Z \varepsilon_0 \varepsilon_m \alpha_e \eta m_z^{B(A)}, \quad (\text{C4})$$

$$p_y^{A(B)} = \varepsilon_0 \varepsilon_m \alpha_e E_{0,y}^{A(B)} + \alpha_e \kappa p_y^{B(A)}, \quad (\text{C5})$$

$$p_z^{A(B)} = \alpha_e \mu p_z^{B(A)} \pm i Z \varepsilon_0 \varepsilon_m \alpha_e \eta m_x^{B(A)}, \quad (\text{C6})$$

where $p_v^{A(B)}$ and $m_v^{A(B)}$ ($v = x, y, \text{ and } z$) represent respectively the three components of the electric and magnetic dipole moments induced in particle A (B); $E_{0,v}$ and $H_{0,v}$ stand for the incident electric and magnetic fields along the three axes. In detail, Eq. (C4) shows that p_x in one particle is excited by the incident electric field $E_{0,x}$ (first term) and the reradiated electric fields by both p_x (second term) and m_z (the third term) in the neighboring particle. Equation (C5) denotes that p_y in one particle is caused by the incident electric field $E_{0,y}$ (first term) and the re-excited electric field by p_y (second term) in the other. Equation (C6) illuminates that p_z in one particle originates from the reradiated electric fields by both p_z (first term) and m_x (second term) in the other particle.

On the other hand, substituting Eqs. (B7) and (B11) into Eq. (A2), the three components of the total magnetic field on particle A (B) are expressed by

$$H_x^{A(B)} = H_0^{A(B)} \pm \frac{i}{Z \varepsilon_0 \varepsilon_s} \eta p_z^{B(A)} + \mu m_x^{B(A)}, \quad (\text{C7})$$

$$H_y^{A(B)} = H_{0,y}^{A(B)} + \kappa m_y^{B(A)}, \quad (\text{C8})$$

$$H_z^{A(B)} = \mp \frac{i}{Z \varepsilon_0 \varepsilon_s} \eta p_x^{B(A)} + \mu m_z^{B(A)}. \quad (\text{C9})$$

Notice that for magnetic field on particle A , the signs of the second term in Eq. (C7) and the first term in Eq. (C9) are respectively positive and negative while they are opposite for particle B . The regulations of the signs are also appropriate for the following Eqs. (C10) and (C12). Owing to the relation $\mathbf{m} = \alpha_m \mathbf{H}$, the three components of the magnetic dipole moment in particle A (B) are determined by

$$m_x^{A(B)} = \alpha_m H_{0,x}^{A(B)} \pm \frac{i}{Z \varepsilon_0 \varepsilon_m} \alpha_m \eta p_z^{B(A)} + \alpha_m \mu m_x^{B(A)}, \quad (\text{C10})$$

$$m_y^{A(B)} = \alpha_m H_{0,y}^{A(B)} + \alpha_m \kappa m_y^{B(A)}, \quad (\text{C11})$$

$$m_z^{A(B)} = \mp \frac{i}{Z \varepsilon_0 \varepsilon_m} \alpha_m \eta p_x^{B(A)} + \alpha_m \mu m_z^{B(A)}. \quad (\text{C12})$$

Equation (C10) shows that m_x in one particle is induced by the incident magnetic field $H_{0,x}$ (first term) and the re-excited magnetic fields by both p_z (second term) and m_x (last term) in the other. Equation (C11) indicates that the m_y in one particle is caused by the incident magnetic field $H_{0,y}$ (first term) and the reradiated magnetic field by m_y (second term) in the neighboring particle. Equation (C12) indicated that m_z in one particle comes from the re-excited magnetic fields by p_x (first term) and m_z (second term) in the neighboring particle. Notice that the p_z and m_z are not directly excited by the incident electric and magnetic fields without a nonzero z component. Equations (C4)–(C6) and (C10)–(C12) demonstrate clearly the hybridizations between the electric and magnetic dipoles in different particles.

APPENDIX D: MATRIX AND SPATIAL PARTIAL DERIVATIVES OF $\vec{\mathbf{G}}_e$ AND $\vec{\mathbf{G}}_m$

For calculating the TOBF, the matrix forms and spatial partial derivatives of $\vec{\mathbf{G}}_e$ and $\vec{\mathbf{G}}_m$ must be known. Substituting the tensors $\mathbf{R}\mathbf{R}/R^2$ and $\vec{\mathbf{I}}$ into Eq. (B3), the matrix of $\vec{\mathbf{G}}_e$ in terms of κ and μ is expressed as

$$\vec{\mathbf{G}}_e = \begin{pmatrix} \mu & 0 & 0 \\ 0 & \kappa & 0 \\ 0 & 0 & \mu \end{pmatrix}. \quad (\text{D1})$$

In addition, based on Eqs. (B3) and (D1), the spatial partial derivatives of $\vec{\mathbf{G}}_e$ with respect to the x and y axes are given by

$$\frac{\partial \vec{\mathbf{G}}_e}{\partial x} = \frac{\kappa - \mu}{R} \begin{pmatrix} 0 & 1 & 0 \\ 1 & 0 & 0 \\ 0 & 0 & 0 \end{pmatrix}, \quad (\text{D2})$$

$$\frac{\partial \vec{\mathbf{G}}_e}{\partial y} = \begin{pmatrix} \partial \mu / \partial R & 0 & 0 \\ 0 & \partial \kappa / \partial R & 0 \\ 0 & 0 & \partial \mu / \partial R \end{pmatrix}. \quad (\text{D3})$$

On the other hand, we have

$$\left(\frac{\mathbf{R} \times \vec{\mathbf{I}}}{R} \right) = \begin{pmatrix} 0 & 0 & -1 \\ 0 & 0 & 0 \\ 1 & 0 & 0 \end{pmatrix}, \quad (\text{D4})$$

where $\mathbf{R} \times \vec{\mathbf{I}}$ denotes the matrix generated by the cross product of \mathbf{R} with each column vector of $\vec{\mathbf{I}}$ [44]. Substituting

Eq. (D4) into Eq. (B8), the matrix of $\vec{\mathbf{G}}_m$ in terms of η is described as

$$\vec{\mathbf{G}}_m = \eta \begin{pmatrix} 0 & 0 & -1 \\ 0 & 0 & 0 \\ 1 & 0 & 0 \end{pmatrix}. \quad (\text{D5})$$

Moreover, based on Eqs. (B8) and (D5), the spatial partial derivative of $\vec{\mathbf{G}}_m$ with respect to the x and y axes are read as

$$\frac{\partial \vec{\mathbf{G}}_m}{\partial x} = \frac{\eta}{R} \begin{pmatrix} 0 & 0 & 0 \\ 0 & 0 & 1 \\ 0 & -1 & 0 \end{pmatrix}, \quad (\text{D6})$$

$$\frac{\partial \vec{\mathbf{G}}_m}{\partial y} = \frac{\partial \eta}{\partial R} \begin{pmatrix} 0 & 0 & -1 \\ 0 & 0 & 0 \\ 1 & 0 & 0 \end{pmatrix}. \quad (\text{D7})$$

Notice that $\partial \vartheta / \partial x = \partial \vartheta / \partial z = 0$ and $\partial \vartheta / \partial y = \partial \vartheta / \partial R$ ($\vartheta = \kappa, \mu$, and η) because R is along the y axis.

APPENDIX E: SPATIAL PARTIAL DERIVATIVE OF TOTAL E^B AND H^B

Let's take particle B as an example. First, Eq. (A13) is decomposed into scalar equations along the three Cartesian axes. Second, Eqs. (D2), (D3), (D6), and (D7) are substituted into the three components of Eq. (A13) while using the relation $\partial \xi_{0,u}^B / \partial x = \partial \xi_{0,u}^A / \partial y = 0$ ($\zeta = E$ and H , $u = x$ and y) for a plane wave propagating along the z axis. Finally, the spatial partial derivatives of the three components of the total electric field in the nearby particle B with respect to the x axis are expressed as

$$\frac{\partial E_x^B}{\partial x} = \frac{\kappa - \mu}{\varepsilon_0 \varepsilon_s R} p_y^A, \quad (\text{E1})$$

$$\frac{\partial E_y^B}{\partial x} = \frac{\kappa - \mu}{\varepsilon_0 \varepsilon_s R} p_x^A + iZ \frac{\eta}{R} m_z^A, \quad (\text{E2})$$

$$\frac{\partial E_z^B}{\partial x} = -iZ \frac{\eta}{R} m_y^A. \quad (\text{E3})$$

In addition, the spatial partial derivatives of the three components of the total electric field along the y axis are written as

$$\frac{\partial E_x^B}{\partial y} = \frac{1}{\varepsilon_0 \varepsilon_s} \frac{\partial \mu}{\partial y} p_x^A - iZ \frac{\partial \eta}{\partial y} m_z^A, \quad (\text{E4})$$

$$\frac{\partial E_y^B}{\partial y} = \frac{1}{\varepsilon_0 \varepsilon_s} \frac{\partial \kappa}{\partial y} p_y^A, \quad (\text{E5})$$

$$\frac{\partial E_z^B}{\partial y} = \frac{1}{\varepsilon_0 \varepsilon_s} \frac{\partial \mu}{\partial y} p_z^A + iZ \frac{\partial \eta}{\partial y} m_x^A. \quad (\text{E6})$$

Analogously, Eq. (A14) is decomposed into scalar equations along the three axes while Eqs. (D2), (D3), (D6), and (D7) are substituted into the three components of Eq. (A14). The spatial partial derivatives of the three components of the total magnetic field in the nearby particle B with respect to the x axis are expressed by

$$\frac{\partial H_x^B}{\partial x} = \frac{\kappa - \mu}{R} m_y^A, \quad (\text{E7})$$

$$\frac{\partial H_y^B}{\partial x} = -\frac{i}{Z \varepsilon_0 \varepsilon_s} \frac{\eta}{R} p_z^A + \frac{\kappa - \mu}{R} m_y^A, \quad (\text{E8})$$

$$\frac{\partial H_z^B}{\partial x} = \frac{i}{Z \varepsilon_0 \varepsilon_s} \frac{\eta}{R} p_y^A. \quad (\text{E9})$$

Meanwhile, the spatial partial derivatives of the three components of the total magnetic field along the y axis are described as

$$\frac{\partial H_x^B}{\partial y} = \frac{i}{Z \varepsilon_0 \varepsilon_s} \frac{\partial \eta}{\partial y} p_z^A + \frac{\partial \mu}{\partial y} m_x^A, \quad (\text{E10})$$

$$\frac{\partial H_y^B}{\partial y} = \frac{\partial \kappa}{\partial y} m_y^A, \quad (\text{E11})$$

$$\frac{\partial H_z^B}{\partial y} = -\frac{i}{Z \varepsilon_0 \varepsilon_s} \frac{\partial \eta}{\partial y} p_x^A + \frac{\partial \mu}{\partial y} m_z^A. \quad (\text{E12})$$

APPENDIX F: TOBF AND TORQUE

By substituting Eqs. (A7)–(A12) and Eqs. (E1)–(E12) into Eq. (A15), the electric component of the binding force along the dimer axis is expressed as

$$F_e = \frac{\varepsilon_0 \varepsilon_s}{2} \left\{ \begin{aligned} & \text{Re} \left[\frac{\partial \kappa}{\partial R} \right] |\tilde{\alpha}_{\text{ey}}|^2 |E_{0,y}|^2 - \text{Re} \left[\frac{\partial \mu}{\partial R} \right] |\tilde{\alpha}_{\text{em-p,1}}|^2 |E_{0,y}|^2 \\ & + \text{Re} \left[\frac{\partial \eta}{\partial R} \tilde{\alpha}_{\text{em-p,2}} \tilde{\alpha}_{\text{em-p,1}}^* \right] |E_{0,y}|^2 \\ & + \text{Re} \left[\frac{\partial \eta}{\partial R} \tilde{\alpha}_{\text{em-s,1}} \tilde{\alpha}_{\text{em-s,2}}^* \right] |E_{0,x}|^2 + \text{Re} \left[\frac{\partial \mu}{\partial R} \right] |\tilde{\alpha}_{\text{em-s,2}}|^2 |E_{0,x}|^2 \end{aligned} \right\}, \quad (\text{F1})$$

the magnetic component of the binding force is expressed as

$$F_m = \frac{\varepsilon_0 \varepsilon_s}{2} \left\{ \begin{aligned} & + \text{Re} \left[\frac{\partial \mu}{\partial R} \right] |\tilde{\alpha}_{\text{em-p,2}}|^2 |E_{0,y}|^2 + \text{Re} \left[\frac{\partial \eta}{\partial R} \tilde{\alpha}_{\text{em-p,1}} \tilde{\alpha}_{\text{em-p,2}}^* \right] |E_{0,y}|^2 \\ & \text{Re} \left[\frac{\partial \kappa}{\partial R} \right] |\tilde{\alpha}_{\text{my}}|^2 |E_{0,x}|^2 - \text{Re} \left[\frac{\partial \mu}{\partial R} \right] |\tilde{\alpha}_{\text{em-s,1}}|^2 |E_{0,x}|^2 \\ & + \text{Re} \left[\frac{\partial \eta}{\partial R} \tilde{\alpha}_{\text{em-s,2}} \tilde{\alpha}_{\text{em-s,1}}^* \right] |E_{0,x}|^2 \end{aligned} \right\}, \quad (\text{F2})$$

and the electric-magnetic coupling component of the binding force is given by

$$F_{\text{em}} = \frac{\varepsilon_0 \varepsilon_s}{12\pi} k^4 \text{Im} [\tilde{\alpha}_{\text{em-p,1}} \tilde{\alpha}_{\text{em-p,2}}^* |E_{0,y}|^2 - \tilde{\alpha}_{\text{em-s,2}} \tilde{\alpha}_{\text{em-s,1}}^* |E_{0,x}|^2]. \quad (\text{F3})$$

On the other hand, the electric component of the torque along the z axis is expressed as

$$\Gamma_e = \frac{\varepsilon_0 \varepsilon_s}{2} \left\{ \begin{aligned} & 2\text{Re} [\kappa - \mu] \text{Re} [\tilde{\alpha}_{\text{em-s,2}} \tilde{\alpha}_{\text{ey}}^* E_{0,x} E_{0,y}^*] \\ & + \text{Re} [\eta (\tilde{\alpha}_{\text{my}} \tilde{\alpha}_{\text{em-p,1}}^* - \tilde{\alpha}_{\text{em-s,2}} \tilde{\alpha}_{\text{ey}}^*) E_{0,x} E_{0,y}^*] \end{aligned} \right\}, \quad (\text{F4})$$

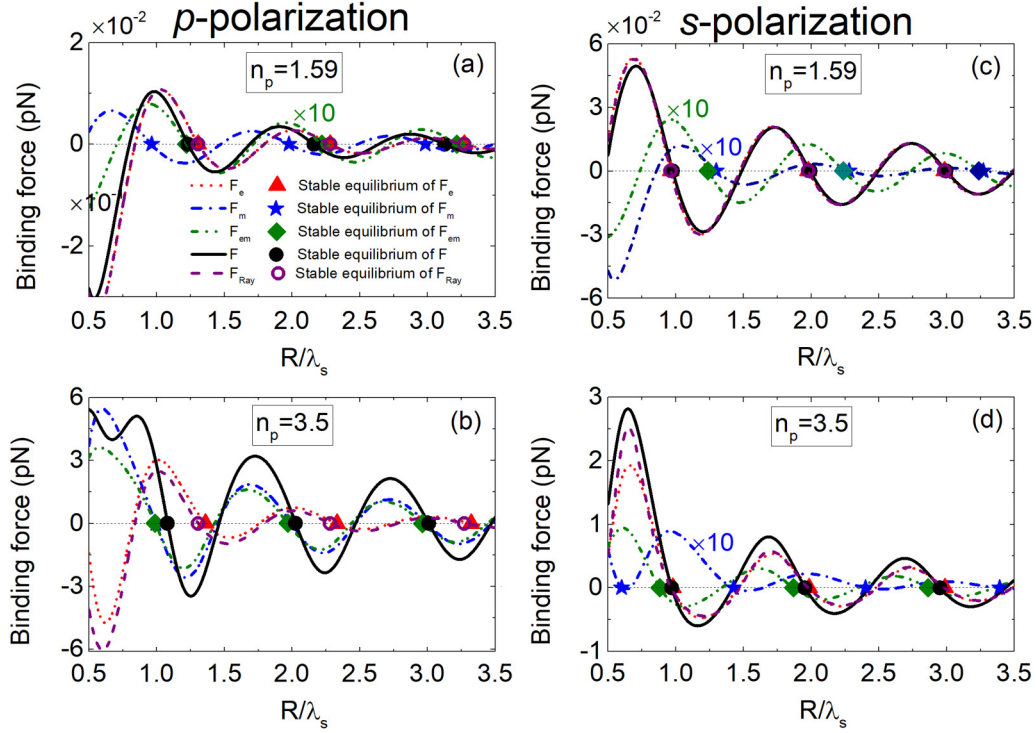


FIG. 5. Binding force upon sphere B with radius 100 nm vs distance (R) between the centers of two spheres with refractive index $n_p = 1.59$ (a),(c) and 3.5 (b),(d) for p polarization (a),(b) and s polarization (c),(d). F (black solid curve) is the binding force while F_e (red short dashed curve), F_m (blue dash-dotted curve), and F_{em} (green dash-dot-dotted curve) are electric, magnetic, and coupling components of F . Additionally, F_{Ray} (purple dashed curve) is the binding force on the same sphere in electric dipolar dimer calculated by the typical Rayleigh approximation [Eq. (3a) in Ref. [15]]. The digits in (a), (c), and (d) indicate a multiple of the magnified force. The solid red triangles, blue stars, green diamonds, black circles, and hollow purple circles represent respectively the stable equilibrium positions of F_e , F_m , F_{em} , F , and F_{Ray} .

the magnetic component of the torque is given by

$$\Gamma_m = \frac{\varepsilon_0 \varepsilon_s}{2} \left\{ \begin{array}{l} -2\text{Re}[\kappa - \mu] \text{Re}[\tilde{\alpha}_{em-p,2} \tilde{\alpha}_{my}^* E_{0,y} E_{0,x}^*] \\ + \text{Re}[\eta(\tilde{\alpha}_{em-p,1} \tilde{\alpha}_{my}^* - \tilde{\alpha}_{ey} \tilde{\alpha}_{em-s,1}^*) E_{0,y} E_{0,x}^*] \end{array} \right\}, \quad (\text{F5})$$

and the electric-magnetic coupling component of the torque is expressed as

$$\Gamma_{em} = \frac{\varepsilon_0 \varepsilon_s}{12\pi} k^4 \text{Im}[(\tilde{\alpha}_{ey} \tilde{\alpha}_{em-s,1}^* + \tilde{\alpha}_{em-p,1} \tilde{\alpha}_{my}^*) E_{0,y} E_{0,x}^*]. \quad (\text{F6})$$

APPENDIX G: BINDING FORCE FOR LOW- AND MODERATE-INDEX PARTICLES

Figure 5(a) shows that F_m (blue dash-dotted curve) and F_{em} (green dash-dot-dotted curve) have nonignorable contributions to F (black solid curve) compared to F_e (red short dashed curve) even for a low-refractive-index dielectric dimer ($n_p = 1.59$), i.e., polystyrene spheres [45] for the p -polarized wave. In detail, although F is mainly determined by F_e when R is smaller than the first stable equilibrium position of F (the first solid black circle on R axis), the contributions of F_m and F_{em} to F cannot be completely ignored. In particular, the first stable equilibrium position of F coincides with the counterpart of F_{em} (the first solid green diamond) instead of that of F_e (the first solid red triangle) even though F_e is an order of magnitude larger than F_{em} . In addition, as R increases, the decay of F_{em} is slower than that of F_m while the decay of F_m is slower than that of F_e . The reasons are the same as in Fig. 2(a) and

as shown in Eqs. (7)–(9) in the main text. The phenomena also exist in Fig. 5(b). Consequently, the contribution of F_m to F is as much as that of F_e , when R goes beyond the first stable equilibrium position of F_e . As a result, the second stable equilibrium position of F (the second solid black circle) diverges from the counterpart of F_{em} (the second solid green diamond) and approaches to the corresponding equilibrium position of F_m (the second solid blue star). This phenomenon is more obvious in the vicinity of the third stable equilibrium position of F (the third solid black point). Additionally, F_{Ray} overlaps completely F_e , while the stable equilibrium positions of F_{Ray} (hollow purple circles) are consistent with those of F_e . The reason is that, for a low-refractive-index dielectric dimer, the hybridization between the two particles is much weaker. It can be seen that F_{em} is an order of magnitude smaller than F_e and F_m . Generally, the x component of magnetic dipole moment m_x in one particle excites the z component of the electric dipole moment p_z in the other due to the hybridization. But this hardly occurs for low-refractive-index particles because of the weak magnetic response. Hence, F_e originates just from the electric dipole-dipole interaction between two particles while each electric dipole is induced by the incident electric field and re-excited electric field of the neighboring electric dipole. The physical mechanism is identical to F_{Ray} .

Interestingly, for particles with moderate refractive index $n_p = 3.5$, i.e., silicon spheres [40], F_m and F_{em} are enhanced

to exceed F_e as shown in Fig. 5(b). As expected, the stable equilibrium positions of F are determined by all components of F , and therefore the positions deviate largely from the corresponding stable equilibrium positions of F_e . Importantly, F has been dramatically strengthened by one order of magnitude compared to the particles with $n_p = 1.59$ in Fig. 5(a). As a result, the stability of the dimer at the stable equilibrium positions is improved by one order of magnitude. The reason is the enhanced magnetic response and hybridization of the dimer with increase of the refractive index of particles. It is worth noting that F_{Ray} overestimates (underestimates) F_e at the first dip (peak) of F_e in front of the first stable equilibrium position of F (see details in Appendix J). Additionally, the stable equilibrium positions of F_e move to large R compared to that of F_{Ray} (hollow purple circles).

Figures 5(c) and 5(d) show the TOBF and its three components for the s -polarized wave. For particles with $n_p = 1.59$ in Fig. 5(c), F_m and F_{em} are an order of magnitude smaller than F_e . Therefore, F is almost completely determined by F_e and the stable equilibrium positions of F and F_e are in agreement. Physically, for an s -polarized wave, the electric dipoles induced in the two particles are side-by-side parallel and directed along the x axis. On the other hand, the y components of the two magnetic dipole induced by both the incident magnetic field and hybridization between them are head-to-tail colinear. As we know, the radiated field by a dipole focuses mainly on the direction perpendicular to the dipole moment. Hence, the radiative interaction between two p_x is stronger than that between two m_y . Additionally, m_z in each particle is caused by the induced p_x in the neighboring one. However, the secondary interaction between two m_z is much smaller than not only the interaction between p_x^A and p_x^B but also the interaction between m_y^A and m_y^B . Furthermore, every corresponding stable equilibrium position of F_e and F_{Ray} overlaps. Meanwhile, the F_e matches completely with F_{Ray} when R exceeds λ_s . The reason is that the two forces originate from the same electric dipolar interaction between p_x^A and p_x^B . What is different, however, than the case of p polarization is that the decay of F_{em} is the slowest while that of F_m is the fastest with increase of R . The reasons are that F_m is proportional to R^{-2} while F_e and F_{em} are proportional to R^{-1} in the far-field region. The phenomena also exist for moderate-refractive-index particles in Fig. 5(d).

With an increase of the refractive index of particles to $n_p = 3.5$ as in Fig. 5(d), F and F_{Ray} are dramatically enhanced by about 50 times compared to Fig. 5(c). As a result, the stability of the dimer at the stable equilibrium positions of F are greatly enhanced the same as the p polarization in Fig. 5(b). In addition, F_{em} is heightened to half of F_e compared to the particle with $n_p = 1.59$ in Fig. 5(c) due to the enhanced hybridization. But F_e is still an order of magnitude larger than F_m because of the unchanged configurations of electric and magnetic dipoles in the dimer. As a result, F is almost determined by both F_e and F_{em} while the stable equilibrium positions of F are nearly dominated by the counterparts of F_e . Notice that F_{Ray} underestimates (overestimates) F_e at the first dip (peak) of F_e although the two forces are coincident at large R , which is contrary to the s polarization in Fig. 5(b) (see details in Appendix H).

APPENDIX H: DIFFERENCE BETWEEN F_e AND F_{Ray} FOR p AND s POLARIZATION

Figure 6 shows F_e together with each of its terms and F_{Ray} as a function of distance (R) between the centers of two spheres with $n_p = 3.5$ for p polarization (a) and s polarization (b). Figure 6(a) shows that F_{Ray} overestimates (underestimates) F_e at the first dip (peak) of F_e in front of the first stable equilibrium position of F for p polarization. From a physical viewpoint, in the vicinity of the dip, the phases of the two p_y in the different particles, which are respectively induced by the incident electric field and the reradiated electric field by the electric dipole in the neighboring particle, are almost synchronous. And then, the two p_y form a head-to-tail colinear configuration and attract each other, the same as the Rayleigh dimer. In addition, the hybridization arises because of the increase of the refractive index of particles. In detail, the m_x in one particle induced by the incident magnetic field excites p_z in the neighboring one. Figure 6(a) shows that the force

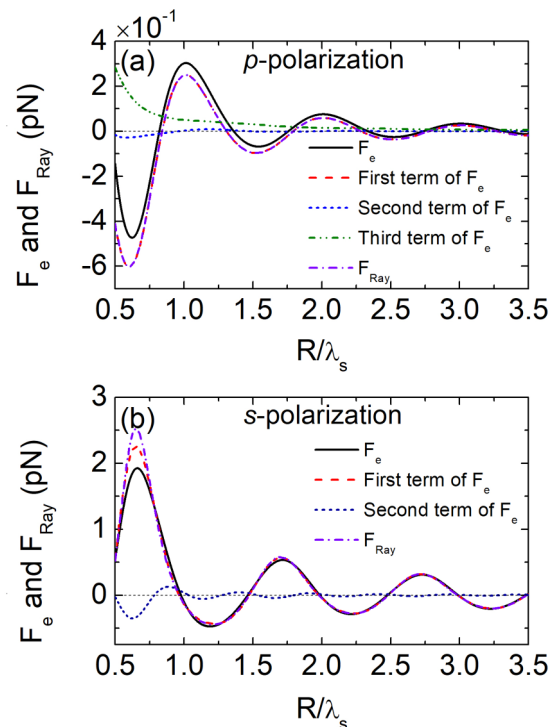


FIG. 6. F_e together with its all terms and F_{Ray} vs distance (R) between the centers of two spheres with refractive index $n_p = 3.5$ for p polarization (a) and s polarization (b). (a) F_e (black solid curve) and F_{Ray} (purple thick dash-dotted curve) are the same as the counterparts in Fig. 5(b). The red dashed, blue short dashed, and green dash-dot-dotted curves are respectively calculated by the first, second, and third terms in Eq. (1) in the main text. Meanwhile, they denote respectively the interactions between p_y^A and p_y^B , between p_z^A and p_z^B , and between p_z^A and m_x^B . (b) F_e and F_{Ray} are the same as the corresponding forces in Fig. 5(d). The red dashed and blue short dashed curves are individually calculated by the fourth and fifth terms in Eq. (1) in the main text. The former denotes the interaction between p_x^A and p_x^B while the latter indicates the interaction between p_x^A and m_z^B . The parameters are the same as in Fig. 2 in the main text.

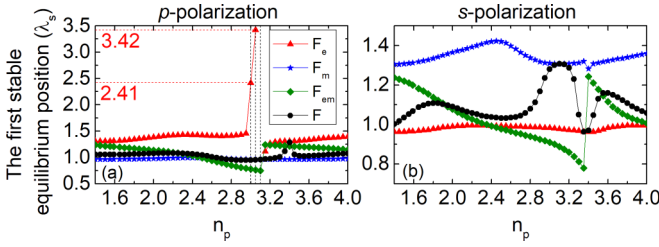


FIG. 7. The first stable equilibrium positions of F (black curve with circles), F_e (red curve with triangles), F_m (blue curve with stars) and F_{em} (green curve with diamonds) vs refractive index (n_p) of the particles for p polarization (a) and s polarization (b). The particle radius is 150 nm. The two horizontal red dashed lines denote the positions $2.41\lambda_s$ and $3.42\lambda_s$. The three vertical black dashed lines in (a) correspond to the locations $n_p = 3, 3.05$, and 3.1 .

due to the interaction between p_y^A and p_y^B (red dashed curve), which is described by the first term in Eq. (1) in the main text, coincides with F_{Ray} (purple thick dash-dotted curve) because of the same physical origin. Additionally, the interaction between p_z^A and m_x^B is repulsive (green dash-dot-dotted curve) while p_z^A and p_z^B are antiparallel and attractive (blue short dashed curve). The two forces are respectively expressed by the third and second terms in Eq. (1) in the main text. But the latter is the secondary interaction and smaller than the former. Therefore the attractive force is partly offset by the repulsive force. It means that the F_e (black solid curve) is reduced by the hybridization compared to F_{Ray} . In a word, F_{Ray} overestimates F_e at the dip of F_e . On the contrary, at the peak of F_e mentioned above, the phases of the two p_y are nearly inverse since the increase of R . This leads to head-to-head colinear configuration of the two p_y . Thus the force due to the interaction between p_y^A and p_y^B (red dashed curve) becomes repulsive while the interaction between p_z^A and m_x^B is still repulsive (green dash-dot-dotted curve). As a result, the repulsive F_e is enhanced which means that F_{Ray} underestimates F_e at the peak of F_e . But the difference between F_e and F_{Ray} is unremarkable at large R because of the weak hybridization.

It is contrary to the p polarization that Fig. 6(b) denotes that F_{Ray} underestimates (overestimates) F_e at the first dip (peak) of F_e in the case of s polarization. This can be also explained by the hybridizations as in the analyses of p polarization. In detail, the reradiated magnetic field by p_x in one particle is strong enough to induce m_z in the neighboring one. On the one hand, the interaction between p_x^A and p_x^B expressed by the fourth term in Eq. (1) in the main text is repulsive (red dashed curve). On the other, the interaction between p_x^A and m_z^B (blue short dashed curve) described by the fifth term in Eq. (1) in the main text is attractive in front of the first peak of F_e . And then the former is partly offset by the latter, which is the reason why F_{Ray} (purple thick dash-dotted curve) is larger than F_e (black solid curve) around the first peaks of F_e . However, the interaction between p_x^A and m_z^B is still attractive when the interaction between p_x^A and p_x^B changes to attraction at the first dip of F_e . As a result, F_e is enhanced and larger than F_{Ray} . As expected, the effects become weaker and weaker with increment of distance (R).

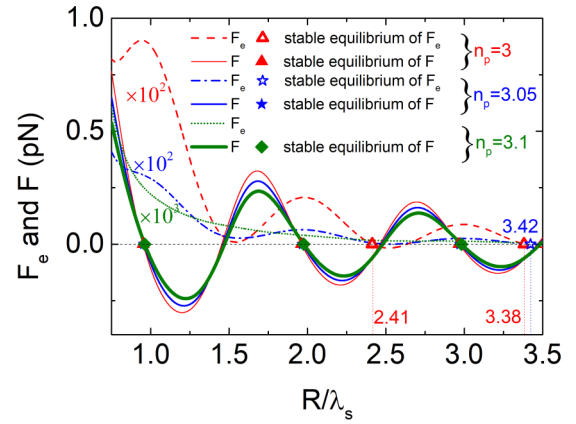


FIG. 8. Binding force F calculated by the sum of Eqs. (1)–(3) in the main text and the electric component F_e , in Eq. (1) vs distance (R) between the centers of two spheres with refractive index $n_p = 3$ (red), 3.05 (blue), and 3.1 (green) for p -polarized wave. The solid thin red, blue, and thick green curves represent individually F for $n_p = 3, 3.05$, and 3.1 . The digits indicate a multiple of the magnified forces. The solid red triangles, blue stars, and green diamonds represent respectively the stable equilibrium positions of F while the hollow red triangles and blue star denote the counterparts of F_e , for $n_p = 3, 3.05$, and 3.1 . The hollow red triangles at positions $R = 2.41\lambda_s$ and $3.38\lambda_s$ denote the first and second stable equilibrium positions of F_e on particles with $n_p = 3$. The hollow blue star at position $R = 3.42\lambda_s$ denotes the unique stable equilibrium position of F_e for particles with $n_p = 3.05$. The solid thick green short-dotted curve corresponding to F_e for $n_p = 3.1$ has no stable equilibrium position. The radius of particle and parameters of both water and wave are same as in Fig. 2 in the main text.

APPENDIX I: STABLE EQUILIBRIUM POSITIONS OF BINDING FORCE IN p AND s POLARIZATIONS

We have calculated the first stable equilibrium positions of F , F_e , F_m , and F_{em} for p and s polarizations. At these positions, the particles experience a restoring force whose intensity is zero and slope is negative. Importantly, the stability of the dimer can be characterized by the stiffness defined as the absolute of the slope of restoring force at the stable equilibrium positions [46]. In general, it is only interesting in the first stable equilibrium position of the binding force because the bound state of the dimer is the most robust at the position due to the maximum stiffness. For p polarization, the first stable equilibrium position of F_e (red curve with triangles) in Fig. 7(a) fluctuates slightly around $1.3\lambda_s$ with increase of n_p . However, the position moves rapidly to $2.41\lambda_s$ and $3.42\lambda_s$ (two horizontal red dashed lines) at locations $n_p = 3$ and 3.05 (left and middle vertical black dashed lines), respectively. Meanwhile, the stiffness of F_e decreases sharply at the two locations, meaning F_e is hardly sufficient to enable the dimer to form a stable bound state. Moreover, the stable equilibrium even vanishes at $n_p = 3.1$ (right vertical black dashed line) where F_e has no stiffness (vertical black dashed line). As expected, F_e without stable equilibrium cannot cause the dimer to form stable configuration at all (see details in Appendix J). On the other hand, the first stable equilibrium position of F_{em} (green curve with diamonds) fluctuates with increase of n_p . Importantly, the first stable equilibrium position of F (black

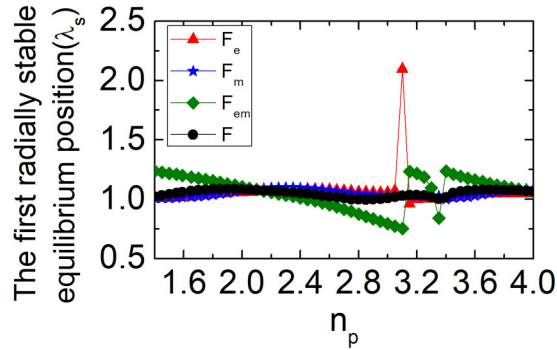


FIG. 9. The first radially stable equilibrium positions of the binding force (F) including all three components (F_e , F_m , and F_{em}) vs refractive index (n_p) of particles for left-circularly polarized wave. The parameters are same as in Fig. 2 in the main text.

curve with circles) is close to the counterpart of F_m (blue curve with stars) around λ_s for all n_p . For s polarization in Fig. 7(b), the stable equilibrium position of F is close to that of F_e and F_{em} in the regions $1.4 < n_p < 2.9$ and $2.5 < n_p < 4$.

APPENDIX J: F AND F_e ON PARTICLE WITH $n_p = 3, 3.05$, AND 3.1 FOR p POLARIZATION

Figure 8 shows F calculated by the sum of Eqs. (1)–(3) in the main text and the electric component F_e in Eq. (1) versus distance (R) between the centers of two spheres with

refractive index $n_p = 3$ (red), 3.05 (blue), and 3.1 (green) for a p -polarized wave. It can be seen that F_e (red dashed and blue dash-dotted curves) has respectively two (red hollow triangle at $2.41\lambda_s$ and $3.38\lambda_s$) and one (blue hollow star at $3.42\lambda_s$) stable equilibrium positions for particles with $n_p = 3$ and 3.05. Meanwhile, F_e is two order of magnitude less than F (blue and thin red solid curves) for both cases of $n_p = 3.05$ and 3. In addition, the stiffness of F_{em} is also far less than that of F [see Fig. 3(a) in the main text]. As a result, F is dominated by F_m . The stable equilibrium positions of F are respectively shown by the solid red triangles and blue stars for $n_p = 3$ and 3.05. Moreover, for particles with $n_p = 3.1$, F_e (green short-dotted curve) is three orders of magnitude less than F (thick green solid curve) and has no stable equilibrium position while the stable equilibrium positions of F (solid green diamonds) are dominated by F_m .

APPENDIX K: RADIALLY STABLE EQUILIBRIUM POSITIONS IN THE CASE OF CIRCULAR POLARIZATION

In the case of circular polarization, the first radially stable equilibrium position of F_{em} (green curve with solid diamonds) in Fig. 9 fluctuates with the increase of n_p while that of F_e (red curve with solid triangles) jumps in the vicinity of $n_p = 3.1$. Interestingly, the corresponding positions of F_m (blue curve with solid stars) and F (black curve with solid circles) are near λ_s and change little. As expected, other stable equilibrium

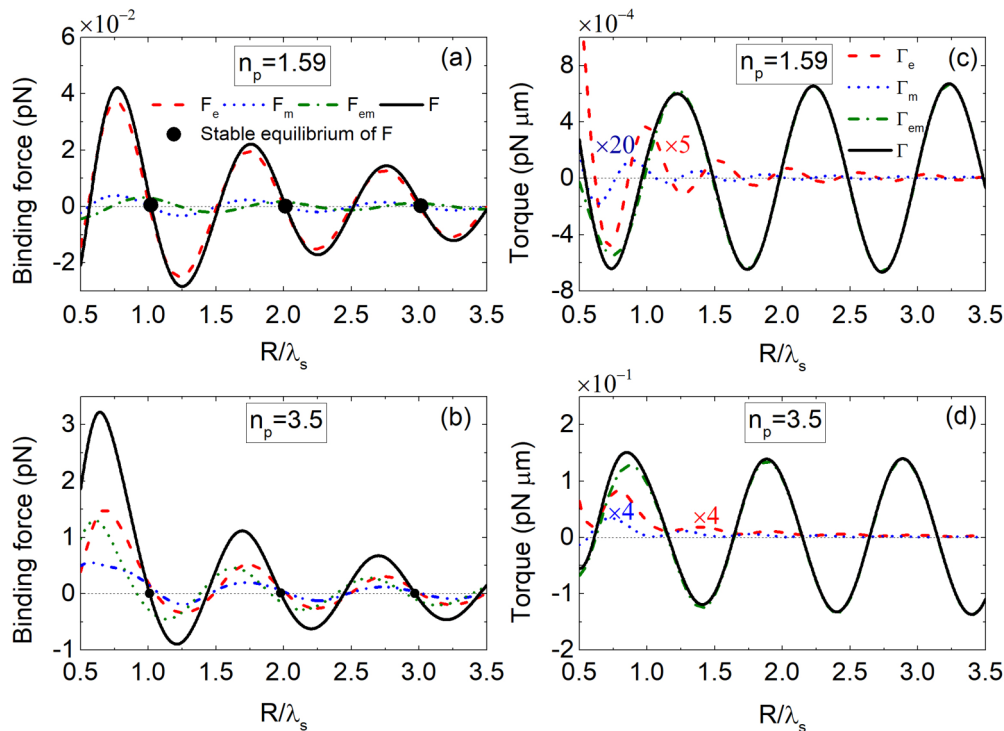


FIG. 10. Binding force and torque on particles for a left-circularly polarized wave. Total binding force (F) and each of the three components (F_e , F_m , and F_{em}) on sphere B vs distance (R), with refractive index $n_p = 1.59$ (a) and 3.5 (b). The solid black circles denote the stable equilibrium positions of F . Total torque (Γ) upon the dimer and each of the three components (Γ_e , Γ_m , and Γ_{em}) vs distance (R) with refractive index $n_p = 1.59$ (c) and 3.5 (d). The digits in (c) and (d) indicate a multiple of the magnified torques. The parameters are the same as in Fig. 2 in the main text.

positions of F lie in near-integer multiples of λ_x while the radial stability of the dimer at the positions decreases in turn.

APPENDIX L: BINDING FORCE AND TORQUE FOR LOW- AND MODERATE-REFRACTIVE-INDEX PARTICLES FOR CIRCULAR POLARIZATION

Figures 10(a) and 10(b) show F_e , F_m , F_{em} , and F with $n_p = 1.59$ and 3.5 for circularly polarized wave. First, for low refractive index in (a), the electric dipole has advantage over the magnetic dipole. And then F_e (red dashed curve) is greatly larger than F_m (blue dash-dot-dotted curve) and F_{em} (green short dashed curve). As a result, F (black solid curve) is mainly dominated by F_e while the stable equilibrium positions of F (black solid circles) are very close to the counterparts of F_e (not marked). This is similar to the p - and s -polarized cases in Figs. 5(a) and 5(c). Second, for moderate refractive index in Fig. 10(b), the electric and magnetic dipoles are effectively induced. Therefore, all components of F are enhanced by two orders of magnitude compared to Fig. 10(a). Naturally, F_e , F_m ,

and F_{em} all contribute non-negligibly to F . As expected, the stable equilibrium positions of F are determined by the F_e , F_m , and F_{em} together.

Figures 10(c) and 10(d) show Γ_e , Γ_m , Γ_{em} , and Γ with $n_p = 1.59$ and 3.5 for the circularly polarized wave. First, even for particles with low refractive index in Fig. 10(c), Γ (black solid curve) is almost dominated by Γ_{em} (green short dashed curve) since Γ_m (blue dash-dot-dotted curve) and Γ_e (red dashed curve) are respectively 20 and 5 times smaller than Γ_{em} . Meanwhile, Γ_m and Γ_e decay with increase of R . Interestingly, the envelopes of Γ_{em} and Γ do not decay as shown by Eqs. (11) and (12) in the main text. Second, for particles with moderate refractive index in Fig. 10(d), Γ and Γ_{em} are dramatically strengthened by three orders of magnitude compared to Fig. 10(c). It means that the increase of refractive index of particles is in favor of torque. In addition, Γ_m is largely enhanced relative to Γ compared to Fig. 10(c). The two facts benefit from the enhanced magnetic response and hybridization of the two particles. Here, Γ is still controlled by Γ_{em} because Γ_{em} is stronger than Γ_e and Γ_m .

-
- [1] K. Dholakia and P. Zemánek, *Rev. Mod. Phys.* **82**, 1767 (2010).
- [2] R. W. Bowman and M. J. Padgett, *Rep. Prog. Phys.* **76**, 026401 (2013).
- [3] M. M. Burns, J.-M. Fournier, and J. A. Golovchenko, *Phys. Rev. Lett.* **63**, 1233 (1989).
- [4] V. Karásek, T. Čížmár, O. Brzobohatý, and P. Zemánek, *Phys. Rev. Lett.* **101**, 143601 (2008).
- [5] I. D. Toftul, D. F. Kornovan, and M. I. Petrov, *ACS Photonics* **7**, 114 (2020).
- [6] M. M. Burns, J.-M. Fournier, and J. A. Golovchenko, *Science* **249**, 749 (1990).
- [7] F. Nan and Z. Yan, *Nano Lett.* **19**, 3353 (2019).
- [8] J. Ng, Z. F. Lin, C. T. Chan, and P. Sheng, *Phys. Rev. B* **72**, 085130 (2005).
- [9] C. D. Mellor, T. A. Fennerty, and C. D. Bain, *Opt. Express* **14**, 10079 (2006).
- [10] T. M. Grzegorzczuk, B. A. Kemp, and J. A. Kong, *Phys. Rev. Lett.* **96**, 113903 (2006).
- [11] Z. Yan, R. A. Shah, G. Chado, S. K. Gray, M. Pelton, and A. N. F. Scherer, *ACS Nano* **7**, 1790 (2013).
- [12] T. M. Grzegorzczuk, J. Rohner, and J.-M. Fournier, *Phys. Rev. Lett.* **112**, 023902 (2014).
- [13] Z. Yan, S. K. Gray, and N. F. Scherer, *Nat. Commun.* **5**, 3751 (2014).
- [14] F. Nan and Z. Yan, *Nano Lett.* **18**, 1396 (2018).
- [15] D. Haefner, S. Sukhov, and A. Dogariu, *Phys. Rev. Lett.* **103**, 173602 (2009).
- [16] N. Sule, Y. Yifat, S. K. Gray, and N. F. Scherer, *Nano Lett.* **17**, 6548 (2017).
- [17] Y. Arita, E. M. Wright, and K. Dholakia, *Optica* **5**, 910 (2018).
- [18] Q. Zhang and J. J. Xiao, *Opt. Lett.* **38**, 4240 (2013).
- [19] Q. Zhang, J. J. Xiao, X. M. Zhang, Y. Yao, and H. Liu, *Opt. Express* **21**, 6601 (2013).
- [20] T.-A. Yano, Y. Tsuchimoto, R. P. Zaccaria, A. Toma, A. Portela, and M. Hara, *Opt. Express* **25**, 431 (2017).
- [21] N. Kostina, M. Petrov, A. Ivinskaya, S. Sukhov, A. Bogdanov, I. Toftul, M. Nieto-Vesperinas, P. Ginzburg, and A. Shalin, *Phys. Rev. B* **99**, 125416 (2019).
- [22] F. Depasse and J.-M. Vigoureux, *J. Phys. D: Appl. Phys.* **27**, 914 (1994).
- [23] R. M. A. Ekeroth, *J. Opt.* **21**, 045001 (2019).
- [24] P. C. Chaumet and A. Rahmani, *Phys. Rev. B* **87**, 195125 (2013).
- [25] A. I. Kuznetsov, A. E. Miroshnichenko, M. L. Brongersma, Y. S. Kivshar, and B. Luk'yanchuk, *Science* **354**, aag2472 (2016).
- [26] W. H. Campos, T. A. Moura, O. J. B. J. Marques, J. M. Fonseca, W. A. Moura-Melo, M. S. Rocha, and J. B. S. Mendes, *Phys. Rev. Res.* **1**, 033119 (2019).
- [27] S. L. Neale, M. P. MacDonald, K. Dholakia, and T. F. Krauss, *Nat. Mater.* **4**, 530 (2005).
- [28] M. J. Crane, E. P. Pandres, E. J. Davis, V. C. Holmberg, and P. J. Pauzauskie, *Nat. Commun.* **10**, 4942 (2019).
- [29] M. Nieto-Vesperinas, J. Sáenz, R. Gómez-Medina, and L. Chantada, *Opt. Express* **18**, 11428 (2010).
- [30] P. Albella, M. A. Poyli, M. K. Schmidt, S. A. Maier, F. Moreno, J. J. Sáenz, and J. Aizpurua, *J. Phys. Chem. C* **117**, 13573 (2013).
- [31] T. Feng, Y. Xu, W. Zhang, and A. E. Miroshnichenko, *Phys. Rev. Lett.* **118**, 173901 (2017).
- [32] C. Guclu, V. A. Tamma, H. K. Wickramasinghe, and F. Capolino, *Phys. Rev. B* **92**, 235111 (2015).
- [33] R. Gómez-Medina, B. García-Cámara, I. Suárez-Lacalle, L. S. Froufe-Pérez, F. González, F. Moreno, M. Nieto-Vesperinas, and J. J. Sáenz, *Photonics Nanostruct. Fundam. Appl.* **10**, 345 (2012).
- [34] P. C. Chaumet and M. Nieto-Vesperinas, *Phys. Rev. B* **64**, 035422 (2001).
- [35] C. F. Bohren and D. R. Huffman, *Absorption and Scattering of Light by Small Particles* (Wiley, New York, 1983).

- [36] R. Gómez-Medina, B. García-Cámara, I. Suárez-Lacalle, F. González, F. Moreno, M. Nieto-Vesperinas, and J. J. Sáenz, *J. Nanophotonics* **5**, 053512 (2011).
- [37] X. Y. Duan and Z. G. Wang, *Phys. Rev. A* **96**, 053811 (2017).
- [38] J. Chen, J. Ng, Z. Lin, and C. Chan, *Nat. Photonics* **5**, 531 (2011).
- [39] L.-M. Zhou, K.-W. Xiao, J. Chen, and N. Zhao, *Laser Photonics Rev.* **11**, 1600284 (2017).
- [40] M. Nieto-Vesperinas, R. Gomez-Medina, and A. J. J. Saenz, *J. Opt. Soc. Am. A* **28**, 54 (2011).
- [41] O. Brzobohatý, T. Čižmár, V. Karásek, M. Šiler, K. Dholakia, and P. Zemánek, *Opt. Express* **18**, 25389 (2010).
- [42] V. Demergis and E.-L. Florin, *Opt. Express* **19**, 20833 (2011).
- [43] N. K. Metzger, E. M. Wright, W. Sibbett, and K. Dholakia, *Opt. Express* **14**, 3677 (2006).
- [44] L. Novotny, B. Hecht, and O. Keller, *Principles of Nano-optics* (Cambridge University Press, New York, 2012).
- [45] O. Brzobohatý, V. Karásek, M. Šiler, L. Chvátal, T. Čižmár, and P. Zemánek, *Nat. Photonics* **7**, 123 (2013).
- [46] A. Ivinskaya, M. I. Petrov, A. A. Bogdanov, I. Shishkin, P. Ginzburg, and A. S. Shalin, *Light Sci. Appl.* **6**, e16258 (2017).